

# Systematic detection of local CH<sub>4</sub> emissions anomalies combining satellite measurements and high-resolution forecasts.

Jérôme Barré<sup>1</sup>, Ilse Aben<sup>2</sup>, Anna Agustí-Panareda<sup>1</sup>, Gianpaolo Balsamo<sup>1</sup>, Nicolas Bousserez<sup>1</sup>, Peter Dueben<sup>1</sup>, Richard Engelen<sup>1</sup>, Antje Inness<sup>1</sup>, Alba Lorente<sup>2</sup>, Joe McNorton<sup>1</sup>, Vincent-Henri Peuch<sup>1</sup>, Gabor Radnoti<sup>1</sup>, Roberto Ribas<sup>1</sup>

<sup>1</sup>ECMWF, European Centre for Medium Range Weather Forecasts, Shinfield Park, Reading, United Kingdom

<sup>2</sup>SRON, Netherlands Institute for Space Research, Utrecht, Netherlands

Correspondence to: Jérôme Barré (jerome.barre@ecmwf.int)

**Abstract.** In this study we present a novel monitoring methodology to detect local CH<sub>4</sub> concentration anomalies worldwide that are related to rapidly changing anthropogenic emissions that significantly contribute to the CH<sub>4</sub> atmospheric budget. The method uses high resolution (7 km x 7 km) retrievals of total column CH<sub>4</sub> from the Tropospheric Monitoring Instrument (TROPOMI) onboard the Sentinel 5 Precursor satellite. Observations are combined with high resolution CH<sub>4</sub> forecasts (~9km) produced by the Copernicus Atmosphere Monitoring Service (CAMS) to provide departures (observations minus forecasts) close to the native satellite resolution at appropriate time. Investigating the departures is an effective way to link satellite measurements and emission inventory data in a quantitative manner. We perform filtering on the departures to remove the large-scale biases on both forecasts and satellite observations. We then use a simple classification on the filtered departures to detect anomalies and plumes coming from CAMS emissions that are missing (e.g. pipeline or facility leaks), under-reported or over-reported (e.g. depleted drilling fields). Additionally, the classification helps to detect local satellite retrieval errors due to land surface albedo issues.

## 1. Introduction

Atmospheric methane (CH<sub>4</sub>) is the second most important anthropogenic greenhouse gas after carbon dioxide and contributes significantly to changes in radiative forcing and climate change. CH<sub>4</sub> is estimated to account for at least a quarter of the present-day warming (Myhre et al., 2013) and has a near-term global warming potential that is 84 times larger than CO<sub>2</sub> per unit mass (IPCC 2013). There are numerous natural and anthropogenic CH<sub>4</sub> sources, which vary in location and areal extent. The anthropogenic emissions related such as oil and gas production and coal mining and biomass burning tends to be geographically localised, e.g. over a plant facility, a pipeline or a field of extraction. Methane emissions however related to biological fluxes such as livestock, landfills and rice fields which can also be either geographically localised over narrow areas



30 or more widespread. For example, microbial respiration in wetlands showing more extensive patterns over the globe (Sauniois  
et al., 2016). Atmospheric methane concentrations have more than doubled since the pre-industrial times because of the  
imbalance between methane sources and sinks (IPCC, 2013), due to an increase of oil and gas production, rice crops, livestock  
and landfills. Methane has a relative short atmospheric lifetime (with respect to climate scales) of around 9 years, meaning  
targeted emission reductions could be an effective way to limit the rate of warming over the upcoming decades (Shoemaker et  
35 al., 2013).

Greenhouse gases emission inventories are generated using aggregation and extrapolation of regional and national specific  
data. These data are reported individually by countries using the guidelines provided by the United Nations Framework on  
Climate Change (UNFCCC) and the Intergovernmental Panel for Climate Change (IPCC). The reporting follows a bottom-up  
approach, which utilises activity data and emission factors of individual emissions sectors. Official reporting and processing  
40 of this data to build these bottom-up inventories can cause significant lag and information can be out of date for certain sectors  
once publicly released. This can become an issue in the context of rapidly changing emissions from large point sources, for  
example in the oil and gas sectors (Alvarez et al., 2018). In the case of atmospheric composition modelling, emission  
inventories are used for input surface fluxes to simulate atmospheric concentrations. Within the Copernicus Atmosphere  
Monitoring Service (CAMS) these simulations are used to provide routine real-time forecasts of greenhouse gases  
45 concentrations. The CAMS greenhouse gas forecasting system integrates satellite observations (Massart et al., 2014, 2016) to  
generate initial conditions for high-resolution forecasts at about 10km (Agustí-Panareda et al., 2019). The lack of up-to-date  
emission inventories will impact and likely degrade simulated CH<sub>4</sub> concentrations in areas where the local contribution of  
anthropogenic emissions is significant.

Many studies have shown the rapidly changing and event-based nature of CH<sub>4</sub> anthropogenic emissions, especially in the  
50 case of identifying the location of 'super-emitter' point source locations. Conley et al. (2016) used aircraft measurements to  
characterise a blowout of a well connected to the Aliso Canyon gas storage facility in California from October 2015 to February  
2016. Pandley et al. (2019) showcased detection of large methane emission from a gas well blowout in Ohio during February  
to March 2018 using satellite measurements. More recently, Varon et al. (2019) detected an anomalously large CH<sub>4</sub> source  
using a combination of satellite instruments over Central Asia (western Turkmenistan) associated with a gas compression  
55 station. Those types of suddenly occurring CH<sub>4</sub> emissions cannot be or are not reported/detected in time to be included in the  
bottom-up inventories but are seen from space. Other studies showed the capability of satellite measurements to detect CH<sub>4</sub>  
emissions related to extensive drilling and fracking areas. Kort et al. (2014) identified a large methane anomaly over the Four  
Corners region of the USA and more recently de Gouw et al. (2020) showed satellite detection of large and extended  
enhancements in the San Juan, Uintah and Permian basin in the USA. While these satellite-based studies focused on specific  
60 events and locations, none of them systematically detected such anomalies at global scale, nor did they provide a method to  
do so.

Systematic detection of large point sources of anthropogenic CH<sub>4</sub> emissions using a combination of satellite observations  
and modelling could enable rapid action to reduce emissions from the oil and gas sectors. Two recent developments allow for



systematic detection of unreported CH<sub>4</sub> atmospheric anomalies linked to small scale and point sources emissions. Firstly,  
65 newly available high resolution (7 km x 7 km) satellite observations from the TROPospheric Monitoring Instrument  
(TROPOMI, Veefkind et al., 2012) on board the Sentinel-5p platform. Secondly, improved real-time forecasting at high-  
resolution (~9 km) provided by CAMS (Agustí-Panareda et al., 2019). In this paper we present a novel methodology to  
routinely compare the satellite observations with the model forecasts in order to perform a systematic detection of atmospheric  
CH<sub>4</sub> anomalies related to emission changes from small scale and point sources emissions that are not reported or lack timely  
70 update. The paper is organised as follows: Section 2 describes the setup that includes the TROPOMI observations, the  
forecasting and monitoring configurations, Section 3 presents the detection method, Section 4 discusses several case studies  
followed by conclusions where we discuss briefly the benefit of our approach with coarse resolution inverse modelling.

## 2. Setup

### 2.1. TROPOMI CH<sub>4</sub> observations

75 The TROPOMI (Veefkind et al., 2012) instrument was launched 13 October 2017 onboard the Sentinel-5 Precursor  
satellite, a low earth orbiter with a Sun-synchronous orbit that overpasses at 13:30 local solar time. Currently operational since  
the end of April 2018, the instrument is an imaging spectrometer with a wide spectral range: ultraviolet, visible, near-infrared  
and shortwave infrared. This allows TROPOMI to measure a variety of atmospheric chemical species such as: ozone, nitrogen  
dioxide, carbon monoxide, sulphur dioxide, formaldehyde, aerosol and methane (Hu et al., 2018). Current CH<sub>4</sub> observations,  
80 which are available for the inner two thirds of the swath and only over land, are vertically integrated columns sensitive to the  
troposphere (surface to 200hPa). With a swath of around 1,750km (normally 2,600 km) wide from the along track position  
and a ground pixel size of 7 km x 7 km, TROPOMI CH<sub>4</sub> data can provide near global daily coverage at high horizontal  
resolution over land but is limited by cloud cover and retrieval quality. In this study, we use the bias corrected version of the  
product and we apply the most stringent quality flagging possible, selecting only pixels that have the *qa\_value* = 1.0 (see  
85 Product Readme Methane V01.03.02, [https://sentinel.esa.int/documents/247904/3541451/Sentinel-5P-Methane-Product-  
Readme-File](https://sentinel.esa.int/documents/247904/3541451/Sentinel-5P-Methane-Product-Readme-File)). Figure 1 illustrates the CH<sub>4</sub> satellite observation coverage that TROPOMI provides over a year, a month and a  
day.

The measurements show clear geographical variation of the CH<sub>4</sub> column-averaged dry-air mixing ratios (XCH<sub>4</sub>) that  
are driven by the atmospheric transport but most importantly by the spatial and temporal variability of the surface fluxes and  
90 emissions variations. Figure 2 shows the 2019 annual average zoomed over the Middle East region and the western USA  
regions. Over these regions, spatial variability results in XCH<sub>4</sub> enhancements of up to 50 ppb over emission  
hotspots. Differences in the average concentrations from region to region are also significant, from approximately 1825 ppb  
over the USA to 1875 ppb over the Middle East. The strong local enhancements are an indication of strong local surface fluxes  
and emissions of CH<sub>4</sub> from oil and gas activities, mining, agriculture or wetlands. XCH<sub>4</sub> retrievals can also be prone to some  
95 systematic residual errors especially related to surface albedo (Hasekamp et al., 2019). De Gouw et al. (2020) for instance



mentioned the possibility of retrieval biases due to low surface albedo in the short wave infrared spectral bands in the winter. Such retrieval biases, even though mostly reduced by the bias corrected product, need further investigation and are outside the scope of this paper. Nevertheless, the TROPOMI data are sufficiently accurate to show local enhancements linked (but not limited) to oil and gas production. We show in section 3 how to isolate these small-scale signals of interest and how to remove the contribution of large-scale biases.

## 2.2. CAMS high-resolution CH<sub>4</sub> forecasting suite

In this study we use the ECMWF Integrated Forecasting System (IFS), which is used in different configurations for the operational Numerical Weather Prediction (NWP) system as well as for the Copernicus Atmosphere Monitoring Service (CAMS) atmospheric composition analyses and forecasts (e.g. Flemming et al, 2015). As part of the CAMS greenhouse gases services, the IFS is used to provide 5 days CO<sub>2</sub> and CH<sub>4</sub> forecasts (Agustí-Panareda et al., 2019) jointly with other species relevant for air-quality (Flemming et al., 2015).

The IFS model cycle used in this paper is CY45R1 and is run routinely with a TCo1279 horizontal resolution which is a cubic octahedral reduced Gaussian grid at approximately 9km (Holm et al., 2016) with 137 vertical levels from the surface to 0.01hPa. Details about the transport and meteorological configuration can be found in Agustí-Panareda et al. (2019). The CAMS greenhouse gases (GHG) operational suite is composed of an analysis and forecasts at medium and high resolution (see Fig. 3). The analysis is based on the IFS 4D-Var assimilation system which was adapted to assimilate retrieved column-averaged mole fractions of CO<sub>2</sub> and CH<sub>4</sub> together with all the operational meteorological observations (Engelen et al., 2009, Massart et al., 2014, 2016). The analyses are produced every 12hours (00:00UTC and 12:00UTC). A 4-day forecast is then issued daily after the 00:00UTC analysis on a TCo399, a cubic octahedral grid corresponding to approximately 25 km x 25 km with the same 137 model level configuration. Two satellite observation streams are currently assimilated, the Infrared Atmospheric Sounding Interferometer (IASI) for CH<sub>4</sub> on the MetOp satellites and the Thermal And Near-infrared Sensor for carbon Observations (TANSO) on the GOSAT satellite for both CO<sub>2</sub> and CH<sub>4</sub> (see Massart et al. (2014) for further details). The processing and acquisition of the level 2 data in 2019 provided the satellite XCH<sub>4</sub> data 4 days behind real time. The high-resolution forecast is then coupled to the analysis experiment by merging the 4-day lower resolution forecast from the CO<sub>2</sub> and CH<sub>4</sub> analysis with the previous 1-day high resolution forecast (Fig. 3) in order to preserve the fine-scale features of the high-resolution forecast. Additionally, the high-resolution forecast coming from the operational NWP runs is used to reset the initial meteorological conditions in order to ensure the best possible accuracy of the transport. In this paper we will focus on using the CH<sub>4</sub> forecasts at high-resolution coming from the setup described above. The high-resolution forecasts are run on a TCo1279 L137 grid of approximately 9 km x 9 km for a 5-day period and are initialized approximately 4 hours behind real-time every day from 00:00UTC.

Both high resolution forecasts and analysis use prescribed CH<sub>4</sub> surface fluxes. The anthropogenic emissions including fossil fuel emissions, agriculture and landfill/waste emissions are from the annual EDGARv4.2FT2010 data set (Olivier and



G. Janssens-Maenhout, 2012) for 2010 with  $0.1^\circ \times 0.1^\circ$  resolution and monthly resolution for the rice emissions (Matthews et al., 1991). Monthly mean wetland emissions come from a climatology (1990-2008) based on the LPJ-WHyMe model  
130 constrained by SCIAMACHY observations during the HYMN project (Spahni et al., 2011) with a resolution of  $1^\circ \times 1^\circ$  degree. The biomass burning emissions are from GFASv1.2 (Kaiser et al., 2012). Other sources and sinks include a monthly soil sink (Ridgwell et al., 1999), annual mean oceanic fluxes (Houweling et al., 1999, Lambert and Schmidt, 1993), and monthly mean fluxes from termites (Sanderson, 1996) and wild animals (Houweling et al., 1999). The chemical sink in the troposphere and the stratosphere is represented by a climatological monthly mean chemical loss rate (Bergamaschi et al., 2009). This is based  
135 on OH fields optimised with methyl chloroform using the TM5 model (Krol et al., 2005) with prescribed concentrations of the stratospheric radicals using the 2-D photochemical Max Planck Institute model. Figure 4 shows the geographical and seasonal structure of the surface fluxes. Large-scale and smoother structures are representative of the wetland, soil and agriculture fluxes, whereas the finer-scale and sharper structures are representative of the anthropogenic and fire emissions.

Figure 5 shows the capability of the high-resolution forecasts at global and regional scales. Global seasonal cycles and  
140 synoptic scale concentrations are represented as well as concentrations at smaller scales such as plumes from point source emissions and orographic effects. Large point sources and associated plumes can be seen over Europe, for example over Madrid, Paris and Tours (western France). Over the Middle East region zoom, sharp point sources are seen in Teheran and Southern Iran as well as over Pakistan (Karachi) and also closer to the Himalayan region.

### 2.3. Monitoring suite

145 To monitor and compare the TROPOMI XCH<sub>4</sub> retrievals with the IFS CH<sub>4</sub> 9 km forecasts we re-use a part of the IFS assimilation system in a so-called monitoring mode. The system recomputes a high-resolution trajectory at 9 km initialised from the forecasts over a 12-hour monitoring window to calculate so-called first guess departures (difference between the observation and the model forecast) with the observations at the appropriate time. At each observation location the departure can be written as follows,

$$150 \quad d = y - \mathbf{HM}(x_i) \quad (1)$$

where  $d$  is the departure,  $y$  the observation,  $\mathbf{H}$  the observation operator,  $\mathbf{M}$  the model integration or trajectory and  $x_i$  the initial CH<sub>4</sub> condition at the beginning of the monitoring window. If we inject the retrieval equation (Rodgers, 2000) the departure becomes,

$$155 \quad d = \mathbf{A}x_t + (\mathbf{I} - \mathbf{A})x_a + \epsilon - \mathbf{AM}(x_i) - (\mathbf{I} - \mathbf{A})x_a \quad (2)$$

where  $x_t$  is the true CH<sub>4</sub> concentration state (which is never exactly known),  $\mathbf{A}$  is the averaging kernel matrix which represents the sensitivity of the retrieval on the vertical profile with respect to the true state,  $\mathbf{I}$  the identity matrix,  $x_a$  the a priori information used in the retrieval and  $\epsilon$  the retrieval error term. The equation then simplifies to,

$$d = \mathbf{A}(x_t - \mathbf{M}(x_i)) + \epsilon \quad (3)$$



160 which is the difference between the true state and the forecast smoothed by the averaging kernel function plus the retrieval  
error term. Those departure values are thus strongly dependent on the averaging kernel function shape. For the TROPOMI  
XCH<sub>4</sub> retrievals the mean averaging kernel function shows a homogenous sensitivity to the entire troposphere up to 200hPa  
where the sensitivity decreases in the stratosphere. The averaging kernel function is not very variable between pixels or  
between different regions of the globe (not shown). Figure 6 shows the departures over various time scales (yearly, monthly  
165 and daily) for the global domain. Overall the departures (observation minus forecast) show a global positive bias of around 25  
ppb (meaning observation values are above the model values) which could be attributed to model biases (Ramonet et al., 2019)  
and/or observation biases (Langerock et al., 2019). Ramonet et al. (2019) compared the CAMS CH<sub>4</sub> forecasts with  
independent total column data. Results showed that the forecasts continuously underestimate the CH<sub>4</sub> total columns by 5-20  
ppb. Langerock et al. (2019) showed that the averaged total column bias for the TROPOMI CH<sub>4</sub> retrievals bias is -0.32% (i.e.  
170 around -5ppb) but with respect to ground-based measurements.

Regional-scale error structures are evident from the observation-model comparison. For example, boreal regions are  
showing a band of negatives values, potentially attributed to systematic errors caused by surface albedo values during winter  
(see section 2.1) in the TROPOMI retrieval algorithm. Alternatively, they could be caused by CH<sub>4</sub> biases at tropopause and  
lower stratosphere levels in the IFS model. Also, a possible time lag in the wetland emissions, which are calculated offline and  
175 provide boundary conditions in the IFS forecasting chain (see section 2.2) could cause such bias. The attribution of this type  
of large-scale error seen in the departures is not fully understood yet and is beyond the scope of this paper, although an  
understanding of these biases is crucial to further improve the quality of the CAMS CH<sub>4</sub> forecasts and TROPOMI retrievals.  
At finer scales, structures are seen on the yearly average comparison and become more evident on the monthly timescales.  
Local differences are even stronger on a daily basis but recognising fine scale structures is challenging due to the lack of daily  
180 coverage. For those reasons a spatial filtering and temporal averaging of the departures is performed to extract and use the  
small-scale features seen in the departures.

### 3. Detection method

#### 3.1. Filtering the signal

To remove the large-scale features seen in the departures we have implemented a high pass Gaussian filtering. The filter  
185 uses a convolution of a 2D Gaussian kernel on a given averaged and binned departure field. In this study we use a 0.1° latitude-  
longitude binning. Due to ocean, cloud cover and quality control flagging a number of bins of the departure will show missing  
values that will jeopardize the convolution. This problem is solved technically by creating two auxiliary matrices that have  
missing values replaced by 0. The two auxiliary matrices are then defined as

$$190 \quad \mathbf{D} = \begin{cases} d_m, & \text{if } n > N \\ 0, & \text{otherwise} \end{cases} \quad (4)$$



$$\mathbf{C} = \begin{cases} 1, & \text{if } n > N \\ 0, & \text{otherwise} \end{cases} \quad (5)$$

where  $d_m$  and is the average departure in the given bin,  $N$  the threshold of minimum number of observations in a given bin. In this study, we have chosen  $N = 2$  in order to avoid smoothing with very isolated pixels that can be faulty but also keep as much data as possible. Replacing the missing values by zeros in  $\mathbf{D}$  introduces an error after convolving (inducing low values due to smoothing out with zeros) in the filtered departures  $d_{lp}$ . This can be compensated by applying the same Gaussian filter on a matrix  $\mathbf{C}$  representing the selected bins for filtering (where number of counts are above  $N$ ) and using the ratio of the two filtered matrices to compensate for the missing value errors. Then a high pass filtering on a given observation space field (here departures) can be formulated as follows,

$$d_{lp} = d - \frac{G(\sigma)*\mathbf{D}}{G(\sigma)*\mathbf{C}} \quad (6)$$

where  $G(\sigma)$  is a 2D Gaussian kernel function with a  $\sigma$  length scale. The same filtering is also applied on the observation values  $y$  and the first guess values  $\mathbf{HM}(x_b)$ . Figure 7 shows the effect of the filtering on the observation-space data using a 30-day window and a length-scale of  $2^\circ$ . Firstly, we can see that the large-scale features in the departures such as the overall bias and regional variations are removed. Secondly, the departures, observations and first guess distributions are put towards gaussianity, centred around zero and displaying more a symmetrical shape and tails. This then makes the processing and the classification of the data much easier (see section 3.2).

To decide on the appropriate window length and Gaussian kernel length scale we have conducted sensitivity tests with different length scales ( $\sigma = [0.5, 1.0, 2.0, 5.0]$  degrees) and a window length of 10, 30 and 90 days. Figure 8 shows the resulting 12 possible sensitivity tests. If the Gaussian kernel is extended, i.e. 5 degrees, large-scale structures tend to be kept in the signal. If the kernel is narrow, i.e.  $0.5^\circ$ , only noise seems to be kept with a few very local minima and maxima. In the latter case too much of the signal contained in the departures seems to be lost. If the time window is short, e.g. 10 days, coverage is low and isolated data points that are spotting possible outliers might be filtered out towards 0. Conversely, if the time window is long, i.e. 90 days, the sharp spatial structures that correspond to more recent or sporadic emission events are smoothed in the time averaging effect and not detected as outliers. For those reasons, we found that a time window of 30 days and a Gaussian kernel of  $2.0^\circ$  provides the most reasonable results.

### 3.2. Outlier classification

The final step is an outlier detection of the filtered departures. We choose to retain the values beyond the  $\pm 3\sigma$  range (ruling out 99.7% of the values). We found that a narrower range retains too many values and starts to fail isolating the important anomalies and conversely a wider range might fail to capture useful information. Further refinements to the current methodology could be done to find an optimal range for outlier detection using more advanced statistical methodologies. In the present study we found that  $\pm 3\sigma$  provides suitable results. In addition to the outlier detection we perform a classification



given the relative values and sign of the filtered observations and first guess values. This allows, us to define the following four categories:

- 225 • **high observations (red in Fig. 9):** where positive filtered observations are higher than filtered first-guess. This class is representative of high XCH<sub>4</sub> values detected by TROPOMI that are not seen as high or at all in the forecasts. These are likely originating from emissions that are not reported or under-estimated in the inventories. However, high observation categorisation may also be caused by poor quality observations category (see section 4.3).
- 230 • **high forecasts (green in Fig. 9):** where positive filtered first-guess are higher than filtered observations. This class is representative of high CH<sub>4</sub> values in the forecasts but not seen as strong or at all in the TROPOMI XCH<sub>4</sub> retrievals. High forecasts categorized data points are likely originating from emissions that are over-estimated or no longer being produced or even mis-located in the emission inventory.
- **low observations (blue in Fig. 9):** where negative filtered observations are lower than filtered first-guess. This class is representative of locally low XCH<sub>4</sub> values detected by TROPOMI but are not seen to be as low or at all in the forecasts. Poor-quality observations influenced by low surface albedo likely fall in that category (see section 4.3).
- 235 • **low forecasts (gold in Fig. 9):** where positive filtered first guess are lower than filtered observations. This class is representative of low XCH<sub>4</sub> values in the forecasts but not seen as low or at all in the TROPOMI XCH<sub>4</sub> retrievals. This category has generally much fewer data points. Orography could be a reason for data points to fall in that category, i.e. model surface height value that are higher than the observation value. Further developments of the method will likely use orography to improve the filtering.

240 In the maps, shades of the colours indicate the intensity of the offset, i.e. how far from perfectly matching observation versus forecasts the filtered departure is. The size of the points indicates the number of samples. A larger dot indicates more data points within the 30-day window to compute the statistics hence is more robust. In the next section we will focus on the under-reported or missed plumes (red) category and over-reported or under-reported plumes (green) category to showcase the usefulness of the method.

## 245 4. Case studies

### 4.1. Under-estimation of local sources in the forecasts

**South Western USA and Mexico:** In figure 9, the method detects under-predicted local CH<sub>4</sub> concentrations (in red) in the forecast system in three areas. This occurs in the Permian Basin region, located around the Texas-New Mexico border, where multiple oil drilling sites are currently operating. Those enhancements have been documented by de Gouw et al. (2020) and Zhang et al, (2020) showing the reliability of the presented method. Two other regions with a smaller bias and extent can be identified around the southern tip of Nevada and northern Baja California close to the US-Mexican border. To our





knowledge those two cases have not been investigated or documented yet. The latter case could be due to local albedo properties that could create local biases in the retrievals (see section 4.3), as we did not identify a facility responsible for those enhancements. This needs further investigation.

255 **Western Turkmenistan:** To confirm the ability of this methodology for the detection of large point-source emitters we also showcase very strong detection of anomalous concentrations over the western Turkmenistan. Our system detects strong enhancement during all of 2019 (Fig.10). The filtered departures can be very large (above 50 ppb) with a high number count in the bins (large size of the dots). As mentioned earlier in this paper, anomalously large CH<sub>4</sub> sources from oil and gas production in this location have been documented and detected using TROPOMI combined with private sector satellite data  
260 by Varon et al. (2019).

#### 4.2. Over estimation of local sources in the forecasts

**Western Russia:** Our detection system shows two local point sources, that show large first-guess values that are not seen by TROPOMI XCH<sub>4</sub> (green dots in Fig. 11). The features do not show large sampling (small dots) in time but do exhibit the shape of plumes, with strong departures near the point sources. One is very close to Moscow and corresponds to the  
265 Domodedovo airport surroundings. The other source detection is near the Volga river with a location matching small drilling fields seen in visible satellite images. In these two locations the detection method suggests that emission inventories are over-estimating local sources, which in reality are now producing reduced emissions or are no longer active emitters (at least during the period of monitoring).

**Los Angeles:** Similar features can occur in the area of Los Angeles. Figure 9 shows significant over-prediction of CH<sub>4</sub>  
270 (green dots) specifically over San Bernardino and Palmdale. Both towns have industrial facilities and regional airports. Strong high forecasted values are also detected in those locations on other dates (not shown) without being seen in the TROPOMI XCH<sub>4</sub> measurements.

Such cases in very different locations show the capability of the method to detect not only missing or underreported point sources but also overreported cases. This can only be achieved with combining numerical models forecasts and satellite  
275 measurements at close-matching high horizontal resolution (9km and 7km respectively). It is also important to mention that the method presented here is subject to uncertainties due to both model transport errors and representation error, although the error associated to emission generally dominate.

#### 4.3. Local retrieval issues

The retrieval can be affected by albedo surface issues (see section 2). The filtering is not able to remove features with  
280 geographical extent smaller than the size of the Gaussian kernel (see section 3.1). Figure 12 presents a typical example of such an issue where the same pattern is seen repeatedly in the outlier detection. This persistent pattern in shape and intensity corresponds to a land surface feature that produces consistently higher TROPOMI XCH<sub>4</sub> values than its surroundings. The inverse can be true as well displaying local areas with consistently lower local XCH<sub>4</sub> retrievals (not shown). Thus, great care



285 should be taken when diagnosing such filtered departures. Features with a consistent shape and intensity are retrieval error artefacts, as atmospheric plumes would show more variability and not a consistent shape over months as illustrated in Fig. 12. Further improvements of the method could be implemented with pattern shape recognition to discard persistent shapes over time. Satellite retrieval providers could be notified about of such biases, in order to improve the quality of the satellite product.

## 5. Conclusions

290 In this paper we have shown the potential of systematic detection of anthropogenic CH<sub>4</sub> point and local source emissions relative to known emission inventory data using the TROPOMI satellite measurements in combination with high resolution CH<sub>4</sub> forecasts. While many studies have shown detailed analysis of a few case studies using TROPOMI observations, this is the first time that a systematic way to detect strong anthropogenic local emitters of CH<sub>4</sub> and to compare results with emission inventories is presented. The method presented here does not only allow for the detection of unreported or missing sources but also targets over-reported sources in the inventories. The method also has the potential of detecting systematic local retrieval 295 errors which can help to improve the satellite product.

Our method is novel by combining information from multiple sources (emission inventory, modelled surface fluxes, and observations) in a data assimilation framework to detect and analyse observed anomalies. We have used global emission inventories and fluxes that were the best possible global estimates we had available at the time when running our system. Using different emission inventories from research specific activities that are more specific to local regions, for instance, could 300 provide different answers. In that way our methodology could provide an efficient way to validate improvements in sector-specific emission inventories. For example, using revised CH<sub>4</sub> inventories such as presented by Maasakers et al. (2016) over the USA or more recently by Scrapelli et al., 2020 globally could lead to different detection patterns. Bottom up inventories will always lag in time and therefore cannot track rapid emission changes such as pipeline and gas facility blowouts. Satellite measurements have a clear added value for timely detection in the case of large emissions.

305 Combining satellite measurements, forecasts and emission inventories partially using a data assimilation system paves the way to estimate the emissions themselves. Inverse modelling studies to estimate CH<sub>4</sub> emissions have been done with SCIAMACHY and GOSAT CH<sub>4</sub> satellite data generally performed at rather low resolution and focus specific study sites (e.g. Jacob et al., 2016). To our knowledge no published studies showed global inversions using TROPOMI data updating emissions close to the 10 km scale globally. Inverse modelling is computationally expensive and in the case of running operations beyond 310 10km scales to close-match satellite observations is a challenge that needs to be overcome over the next decade. Efforts are underway to implement a sector-specific inverse high-resolution modelling monitoring system as part of the CAMS service evolution at ECMWF and the future Copernicus CO<sub>2</sub> service at global and regional scales (e.g. Barré et al., 2019, Bousseret et al., 2019, Pinty et al., 2019, Janssens-Maenhout et al., 2020). Approaches combining global and regional modelling could be adopted to perform inversion at fine scales but at the cost of missing fine-scale detection outside the regional domains. 315 Large and local CH<sub>4</sub> emissions events could occur in very remote areas, which are typically not considered in regional



modelling setups (e.g. West Turkmenistan, Varon et al., 2019). Systematic detection will then require setting up many regional subdomains leading again to computational burden for a single monitoring entity. We have demonstrated that monitoring of satellite XCH<sub>4</sub> departures at high resolution at global scale using already existing parts of a forecasting chain remains an affordable solution to develop a much needed capability: tracking rapidly changing CH<sub>4</sub> sources across the world and support the urgently needed effort on developing climate policies for reducing anthropogenic CH<sub>4</sub> emissions.

## References

- Agustí-Panareda, A., Diamantakis, M., Massart, S., Chevallier, F., Muñoz-Sabater, J., Barré, J., Curcoll, R., Engelen, R., Langerock, B., Law, R. M., Loh, Z., Morguí, J. A., Parrington, M., Peuch, V.-H., Ramonet, M., Roehl, C., Vermeulen, A. T.,  
325 Warneke, T., and Wunch, D.: Modelling CO<sub>2</sub> weather – why horizontal resolution matters, *Atmos. Chem. Phys.*, 19, 7347–7376, <https://doi.org/10.5194/acp-19-7347-2019>, 2019.
- Alvarez, R. A., Zavala-Araiza, D., Lyon, D. R., Allen, D. T., Barkley, Z. R., Brandt, et al. (2018). Assessment of methane emissions from the U.S. oil and gas supply chain. *Science*, 361, 186–188. <https://doi.org/10.1126/science.aar7204>
- 330 Bergamaschi, P., Frankenberg, C., Meirink, J. F., Krol, M., Villani, M. G., Houweling, S., Dentener, F., Dlugokencky, E. J., Miller, J. B., Gatti, L. V., Engel, A., and Levin, I. (2009). Inverse modeling of global and regional CH<sub>4</sub> emissions using SCIAMACHY satellite retrievals. *J. Geophys. Res.*, 114.
- Barré J., Massart S., Ades M., Jones L., and Engelen R. (2019)., Emission optimisations first attempt based on Ensemble of  
335 DA for atmospheric composition, ECMWF technical memoranda, <https://doi.org/10.21957/4grkg5ga0>
- Bousserez, N., 2019. Towards a Prototype Global CO<sub>2</sub> Emissions Monitoring System for Copernicus. *arXiv preprint arXiv:1910.11727*.
- Conley, S., Franco, G., Faloona, I., Blake, D. R., Peischl, J., & Ryerson, T. B. (2016). Methane emissions from the 2015 Aliso  
340 Canyon blowout in Los Angeles, CA. *Science*, 351, 1317–1320. <https://doi.org/10.1126/science.aaf2348>
- de Gouw, J.A., Veefkind, J.P., Roosenbrand, E. et al. Daily Satellite Observations of Methane from Oil and Gas Production Regions in the United States. *Sci Rep* 10, 1379 (2020). <https://doi.org/10.1038/s41598-020-57678-4>
- Engelen, R. J., Serrar, S., and Chevallier, F. (2009), Four-dimensional data assimilation of atmospheric CO<sub>2</sub> using AIRS observations, *J. 114*, D03303, doi:[10.1029/2008JD010739](https://doi.org/10.1029/2008JD010739).
- 345 Flemming, J., Huijnen, V., Arteta, J., Bechtold, P., Beljaars, A., Blechschmidt, A.-M., Diamantakis, M., Engelen, R. J., Gaudel, A., Inness, A., Jones, L., Josse, B., Katragkou, E., Marecal, V., Peuch, V.-H., Richter, A., Schultz, M. G., Stein, O., and



- Tsikerdekis, A.: Tropospheric chemistry in the Integrated Forecasting System of ECMWF, *Geosci. Model Dev.*, 8, 975–1003, <https://doi.org/10.5194/gmd-8-975-2015>, 2015.
- 350 Hasekamp, O., Lorente, A., Hu, H., Butz, A., aan de Brugh, J., and Landgraf, J., Algorithm Theoretical Baseline Document for Sentinel-5 Precursor Methane retrieval, SRON-S5P-LEV2-RP-001, <https://sentinel.esa.int/documents/247904/2476257/Sentinel-5P-TROPOMI-ATBD-Methane-retrieval>, 2019
- Holm, E., Forbes, R., Lang, S., Magnusson, L., and Malardel, S.: New model cycle brings higher resolution, ECMWF  
355 Newsletter, No. 147, available at: <https://www.ecmwf.int/en/elibrary/16299-newsletter-no-147-spring-2016> (last access: 30 May 2019), 2016. a, b
- Houweling, S., Kaminski, T., Dentener, F., Lelieveld, J., and Heimann, M.: Inverse modeling of methane sources and sinks using the adjoint of a global transport model, *J. Geophys. Res.*, 104, 26137–26160, doi:10.1029/1999JD900428, 1999
- 360 Hu, H., Landgraf, J., Detmers, R., Borsdorff, T., Aan de Brugh, J., Aben, I., et al. (2018). Toward global mapping of methane with TROPOMI: First results and intersatellite comparison to GOSAT. *Geophysical Research Letters*, 45, 3682–3689. <https://doi.org/10.1002/2018GL077259>
- IPCC. Observations: Atmosphere and Surface (2013).
- 365 Jacob, D. J., Turner, A. J., Maasakkers, J. D., Sheng, J., Sun, K., Liu, X., Chance, K., Aben, I., McKeever, J., & Frankenberg, C. (2016). Satellite observations of atmospheric methane and their value for quantifying methane emissions. *Atmospheric Chemistry and Physics*, 16(22), 14,371–14,396. <https://doi.org/10.5194/acp-16-14371-2016>
- 370 Janssens-Maenhout, G., B. Pinty, M. Dowell, H. Zunker, E. Andersson, G. Balsamo, J.-L. Bézy, T. Brunhes, H. Bösch, B. Bojkov, D. Brunner, M. Buchwitz, D. Crisp, P. Ciais, P. Counet, D. Dee, H. Denier van der Gon, H. Dolman, M. Drinkwater, O. Dubovik, R. Engelen, T. Fehr, V. Fernandez, M. Heimann, K. Holmlund, S. Houweling, R. Husband, O. Juvyns, A. Kentarchos, J. Landgraf, R. Lang, A. Löscher, J. Marshall, Y. Meijer, M. Nakajima, P.I. Palmer, P. Peylin, P. Rayner, M. Scholze, B. Sierk, J. Tamminen, P. Veeffkind, Towards an operational anthropogenic CO<sub>2</sub> emissions monitoring and  
375 verification support capacity, *Bulletin of the American Meteorological Society* (accepted), 2020, doi: 10.1175/BAMS-D-19-0017.1
- Kaiser, J. W., Heil, A., Andreae, M. O., Benedetti, A., Chubarova, N., Jones, L., Morcrette, J.-J., Razinger, M., Schultz, M. G., Suttie, M., and van der Werf, G. R.: Biomass burning emissions estimated with a global fire assimilation system based on  
380 observed fire radiative power, *Biogeosciences*, 9, 527–554, <https://doi.org/10.5194/bg-9-527-2012>, 2012.



- Kirschke, S., Bousquet, P., Ciais, P. *et al.* Three decades of global methane sources and sinks. *Nature Geosci* 6, 813–823 (2013). <https://doi.org/10.1038/ngeo1955>
- 385 Kort, E. A., Frankenberg, C., Costigan, K. R., Lindenmaier, R., Dubey, M. K., and Wunch, D. (2014), Four corners: The largest US methane anomaly viewed from space, *Geophys. Res. Lett.*, 41, 6898–6903, doi:10.1002/2014GL061503.
- Krol, M., Houweling, S., Bregman, B., van den Broek, M., Segers, A., van Velthoven, P., Peters, W., Dentener, F., and Bergamaschi, P.: The two-way nested global chemistry-transport zoommodel TM5: algorithm and applications, *Atmos. Chem. Phys.*, 5, 417–432, doi:10.5194/acp-5-417-2005, 2005.
- 390 Lambert, G. and Schmidt, S.: Reevaluation of the oceanic flux of methane: uncertainties and long term variations, *Chemosph. Global Change Sci.*, 26, 579–589, 1993
- Langerock B., Kumar M., Lambert J., Lorente A. and Landgraf J., First comparison results for the S5P CH<sub>4</sub> product based on correlative reference measurements acquired by FTIR instruments contributing to NDACC and TCCON networks. [http://mpc-vdaf.tropomi.eu/ProjectDir/reports/pdf/S5P-MPC-VDAF-VWA-L2\\_CH4\\_20190301.pdf](http://mpc-vdaf.tropomi.eu/ProjectDir/reports/pdf/S5P-MPC-VDAF-VWA-L2_CH4_20190301.pdf)
- 395
- Maasackers, Joannes D., Daniel J. Jacob, Melissa P. Sulprizio, Alexander J. Turner, Melissa Weitz, Tom Wirth, Cate Hight, Mark Degrep ueiredo, Mausami Desai, Rachel Schmeltz, Leif Hockstad, Anthony A. Bloom, Kevin W. Bowman, Seongeun Jeong, and Marc L. Fischer: Gridded National Inventory of U.S. Methane Emissions *Environmental Science & Technology* 2016 50 (23), 13123–13133, DOI: 10.1021/acs.est.6b02878
- 400
- Massart, S., Agustí-Panareda, A., Aben, I., Butz, A., Chevallier, F., Crevoisier, C., Engelen, R., Frankenberg, C., and Hasekamp, O.: Assimilation of atmospheric methane products into the MACC-II system: from SCIAMACHY to TANSO and IASI, *Atmos. Chem. Phys.*, 14, 6139–6158, <https://doi.org/10.5194/acp-14-6139-2014>, 2014.
- 405
- Massart, S., Agustí-Panareda, A., Heymann, J., Buchwitz, M., Chevallier, F., Reuter, M., Hilker, M., Burrows, J. P., Deutscher, N. M., Feist, D. G., Hase, F., Sussmann, R., Desmet, F., Dubey, M. K., Griffith, D. W. T., Kivi, R., Petri, C., Schneider, M., and Velasco, V. A.: Ability of the 4-D-Var analysis of the GOSAT BESD XCO<sub>2</sub> retrievals to characterize atmospheric CO<sub>2</sub> at large and synoptic scales, *Atmos. Chem. Phys.*, 16, 1653–1671, <https://doi.org/10.5194/acp-16-1653-2016>, 2016.
- 410
- Matthews, E., Fung, I., and Lerner, J.: Methane emission from rice cultivation: geographic and seasonal distribution of cultivated areas and emissions, *Global Biogeochem. Cy.*, 5, 3–24, doi:10.1029/90GB02311, 1991



Myhre G. et al., “Anthropogenic and natural radiative forcing” in Climate Change 2013: The Physical Science Basis.  
415 Contribution of Working Group I to the Fifth Assessment Report of the Intergovernmental Panel on Climate Change, T. F. Stocker et al., Eds. (Cambridge University Press, Cambridge, United Kingdom, 2013), pp. 659–740.

Olivier and G. Janssens-Maenhout, CO<sub>2</sub> Emissions from Fuel Combustion -- 2012 Edition, IEA CO<sub>2</sub> report 2012, Part III, Greenhouse-Gas Emissions, ISBN 978-92-64-17475-7

420

Pandey S., Ritesh Gautam, Sander Houweling, Hugo Denier van der Gon, Pankaj Sadavarte, Tobias Borsdorff, Otto Hasekamp, Jochen Landgraf, Paul Tol, Tim van Kempen, Ruud Hoogeveen, Richard van Hees, Steven P. Hamburg, Joannes D. Maasackers and Ilse Aben, Satellite observations reveal extreme methane leakage from a natural gas well blowout, *Proceedings of the National Academy of Sciences*, <https://doi.org/10.1073/pnas.1908712116>, (201908712), (2019).

425

Pinty B., P. Ciais, D. Dee, H. Dolman, M. Dowell, R. Engelen, K. Holmlund, G. Janssens-Maenhout, Y. Meijer, P. Palmer, M. Scholze, H. Denier van der Gon, M. Heimann, O. Juvyns, A. Kentarchos and H. Zunker (2019) An Operational Anthropogenic CO<sub>2</sub> Emissions Monitoring & Verification Support Capacity – Needs and high level requirements for in situ measurements, doi: 10.2760/182790, European Commission Joint Research Centre, EUR 29817 EN.

430

Ramonet, M., A. Wagner, M. Schulz, Y. Christophe, H. J. Eskes, S. Basart, A. Benedictow, Y. Bennouna, A.-M. Blechschmidt, S. Chabrillat, E. Cuevas, A. ElYazidi, H. Flentje, K.M. Hansen, U. Im, J. Kapsomenakis, B. Langerock, A. Richter, N. Sudarchikova, V. Thouret, T. Warneke, C. Zerefos, Validation report of the CAMS near-real-time global atmospheric composition service: Period June - August 2019, Copernicus Atmosphere Monitoring Service (CAMS) report,  
435 CAMS84\_2018SC1\_D1.1.1\_JJA2019\_v1.pdf, November 2019, doi:10.24380/def9-na43.

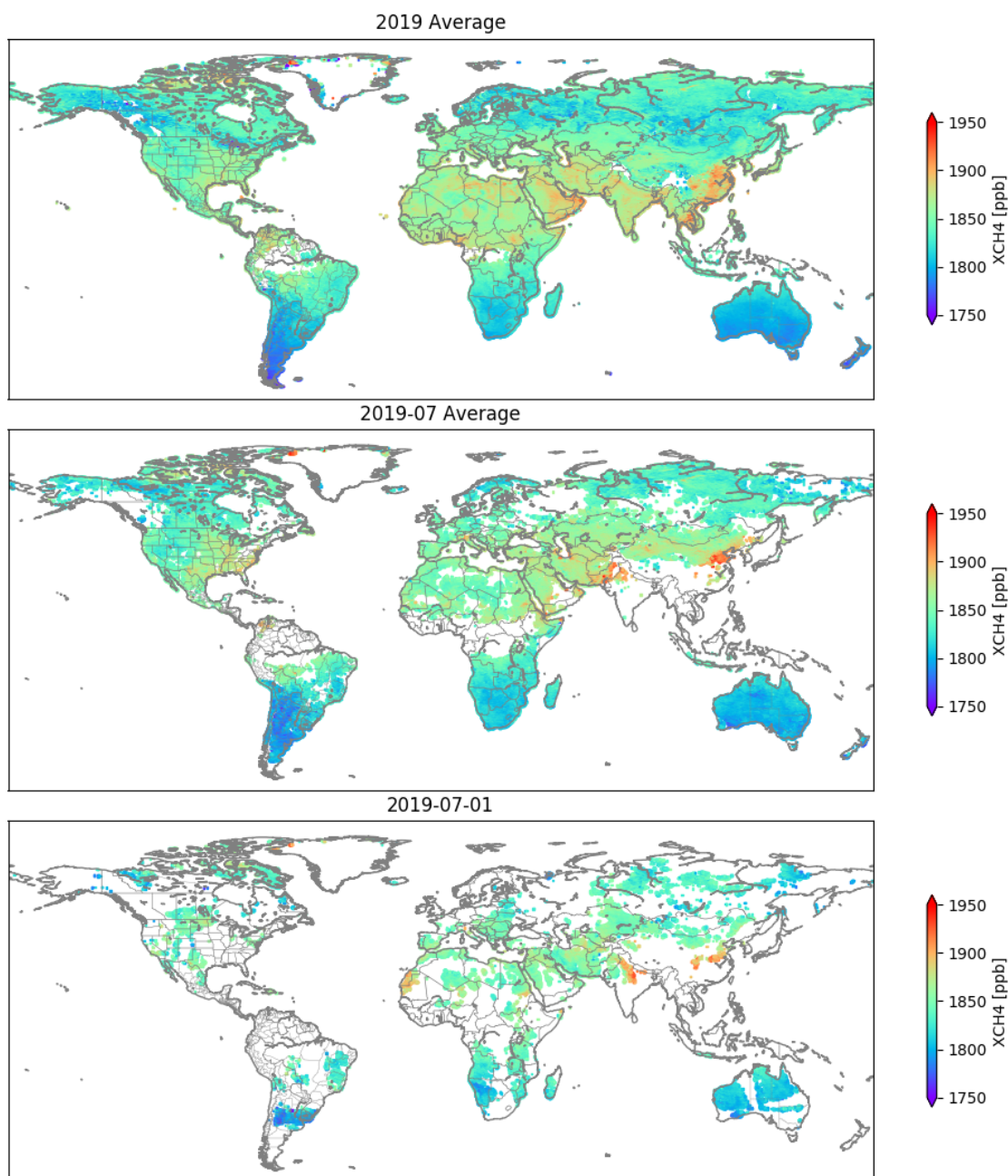
Ridgwell, A. J., Marshall, S. J., and Gregson, K.: Consumption of atmospheric methane by soils: a process-based model, *Global Biogeochem. Cy.*, 13, 59–70, doi:10.1029/1998GB900004, 1999

Sanderson, M. G.: Biomass of termites and their emissions of methane and carbon dioxide: a global database, *Global Biogeochem. Cy.*, 10, 543–557, doi:10.1029/96GB01893

Saunois, M., Bousquet, P., Poulter, B., Peregón, A., Ciais, P., Canadell, J. G., Dlugokencky, E. J., Etiope, G., Bastviken, D., Houweling, S., Janssens-Maenhout, G., Tubiello, F. N., Castaldi, S., Jackson, R. B., Alexe, M., Arora, V. K., Beerling, D.  
445 J., Bergamaschi, P., Blake, D. R., Brailsford, G., Brovkin, V., Bruhwiler, L., Crevoisier, C., Crill, P., Covey, K., Curry, C., Frankenberg, C., Gedney, N., Höglund-Isaksson, L., Ishizawa, M., Ito, A., Joos, F., Kim, H. S., Kleinen, T., Krummel, P., Lamarque, J. F., Langenfelds, R., Locatelli, R., Machida, T., Maksyutov, S., McDonald, K. C., Marshall, J., Melton, J.

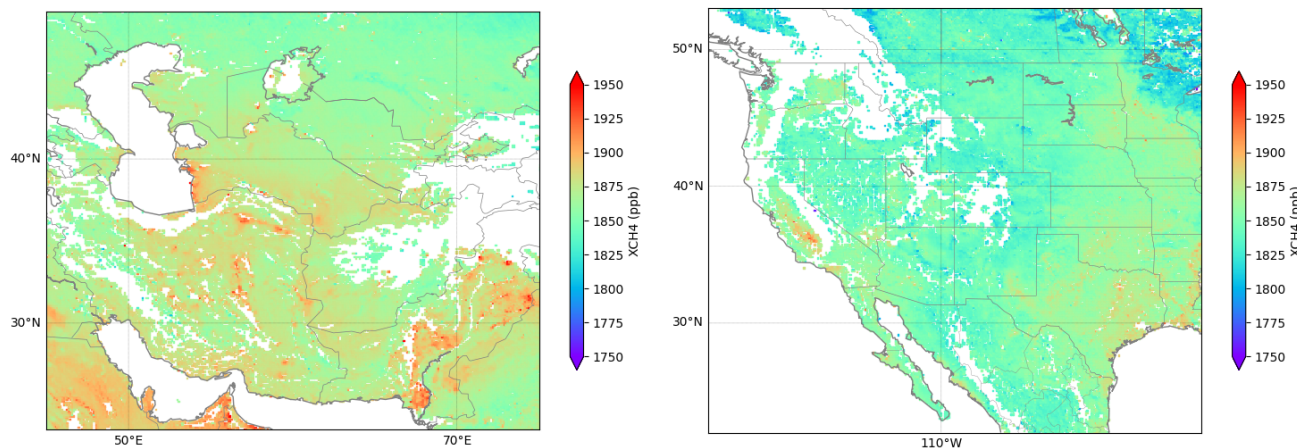


- R., Morino, I., Naik, V., O'Doherty, S., Parmentier, F. J. W., Patra, P. K., Peng, C., Peng, S., Peters, G. P., Pison, I., Prigent, C., Prinn, R., Ramonet, M., Riley, W. J., Saito, M., Santini, M., Schroeder, R., Simpson, I. J., Spahni, R., Steele, P., Takizawa, A., Thornton, B. F., Tian, H., Tohjima, Y., Viovy, N., Voulgarakis, A., vanWeele, M., van der Werf, G. R., Weiss, R., Wiedinmyer, C., Wilton, D. J., Wiltshire, A., Worthly, D., Wunch, D., Xu, X., Yoshida, Y., Zhang, B., Zhang, Z., & Zhu, Q. (2016). The global methane budget 2000–2012. *Earth System Science Data*, 8( 2), 697– 751. <https://doi.org/10.5194/essd-8-697-2016>
- 455 Shoemaker J. K., D. P. Schrag, M. J. Molina, V. Ramanathan, Climate change. What role for short-lived climate pollutants in mitigation policy? *Science* 342, 1323–1324 (2013).
- Spahni, R., Wania, R., Neef, L., van Weele, M., Pison, I., Bousquet, P., Frankenberg, C., Foster, P. N., Joos, F., Prentice, I. C., and van Velthoven, P.: Constraining global methane emissions and uptake by ecosystems, *Biogeosciences*, 8, 1643–1665, <https://doi.org/10.5194/bg-8-1643-2011>, 2011.
- Scarpelli, T. R., Jacob, D. J., Maasackers, J. D., Sulprizio, M. P., Sheng, J.-X., Rose, K., Romeo, L., Worden, J. R., and Janssens-Maenhout, G.: A global gridded ( $0.1^\circ \times 0.1^\circ$ ) inventory of methane emissions from oil, gas, and coal exploitation based on national reports to the United Nations Framework Convention on Climate Change, *Earth Syst. Sci. Data*, 12, 563–575, <https://doi.org/10.5194/essd-12-563-2020>, 2020.
- 465 575, <https://doi.org/10.5194/essd-12-563-2020>, 2020.
- Varon, D. J., Jacob, D. J., McKeever, J., Jervis, D., Durak, B. O. A., Xia, Y., & Huang, Y. (2018). Quantifying methane point sources from fine-scale satellite observations of atmospheric methane plumes. *Atmospheric Measurement Techniques*, 11, 5673–5686. <https://doi.org/10.5194/amt-11-5673-2018>
- 470 5686. <https://doi.org/10.5194/amt-11-5673-2018>
- Varon, D. J., McKeever, J., Jervis, D., Maasackers, J. D., Pandey, S., Houweling, S., et al. (2019). Satellite discovery of anomalously large methane point sources from oil/gas production. *Geophysical Research Letters*, 46, 13507– 13516. <https://doi.org/10.1029/2019GL083798>
- 475 13507– 13516. <https://doi.org/10.1029/2019GL083798>
- Veefkind, J. P., Aben, I., McMullan, K., Förster, H., de Vries, J., Otter, G., et al. (2012). TROPOMI on the ESA Sentinel-5 Precursor: A GMES mission for global observations of the atmospheric composition for climate, air quality and ozone layer applications. *Remote Sensing of Environment*, 120, 70–83. <https://doi.org/10.1016/j.rse.2011.09.027>
- 480 Zhang, Y., Gautam, R., Pandey, S., Omara, M., Maarakkers, J. D., Sadavarte, P., et al, Quantifying methane emissions from the largest oil-producing basin in the United States from space, *Science Advances*, doi: 10.1126/sciadv.aaz5120 (2020)

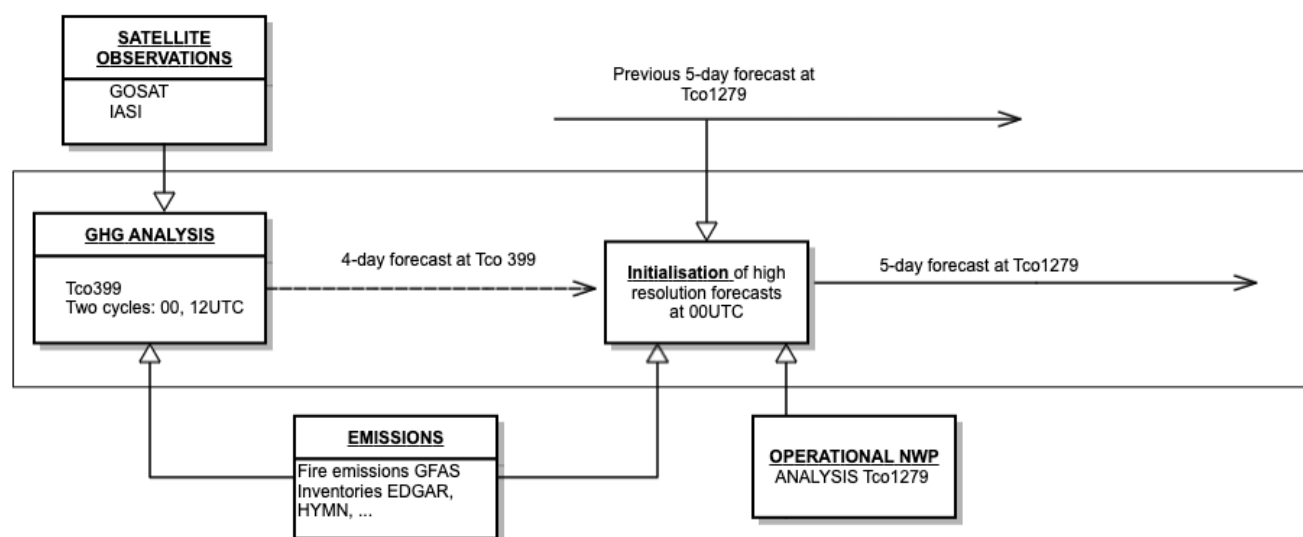


485 **Figure 1. Global average of TROPOMI XCH<sub>4</sub> column-averaged dry-air mixing ratios for the full year 2019, July 2019 and July 1st, 2019 (top to bottom).**





490 **Fig 2. Regional zooms of TROPOMI XCH<sub>4</sub> columns for the full year 2019. Middle East (left) and Central-Western North America (right).**



495 **Figure 3. Flow chart of the CAMS greenhouse gas analysis and forecast system.**

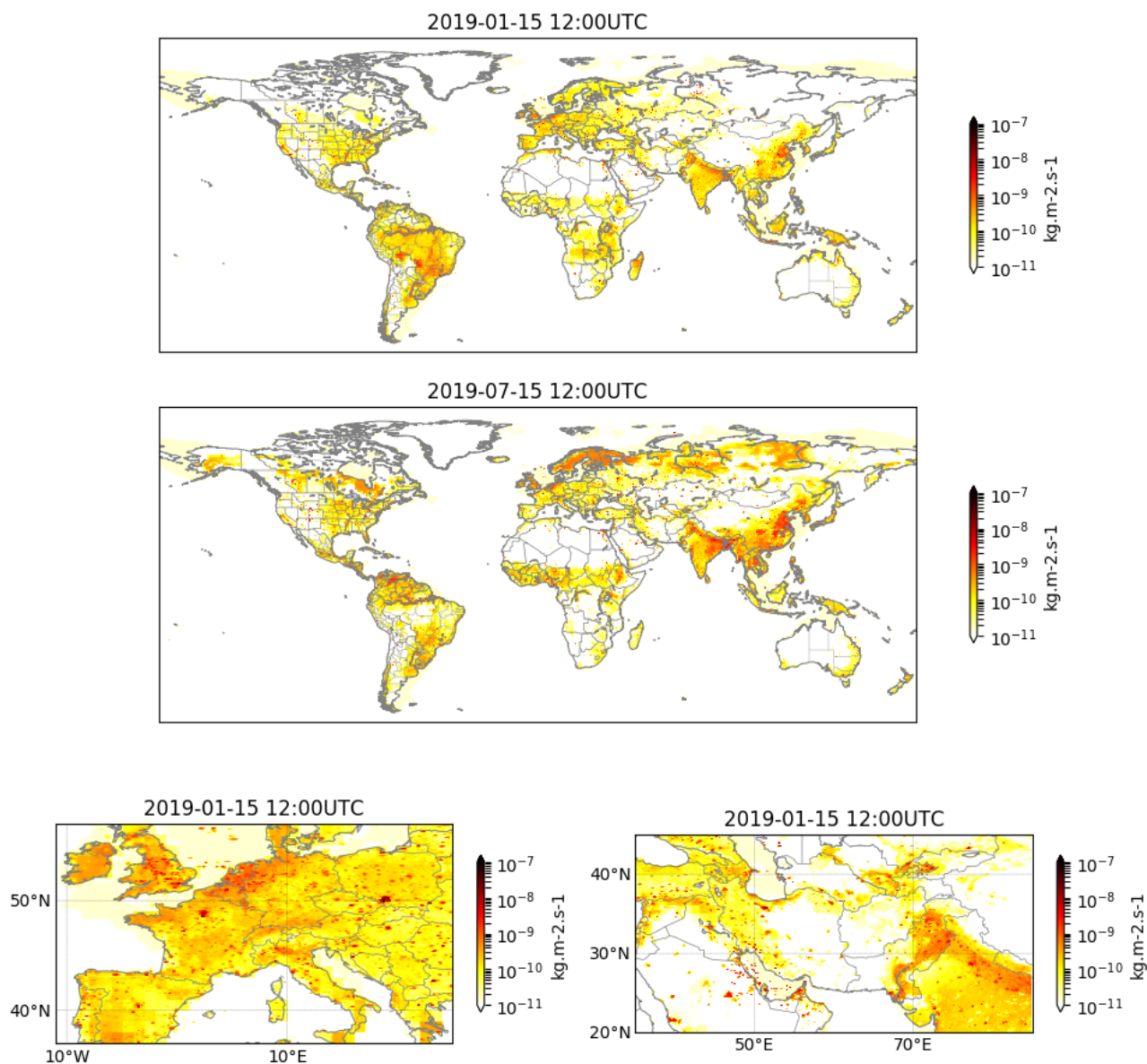
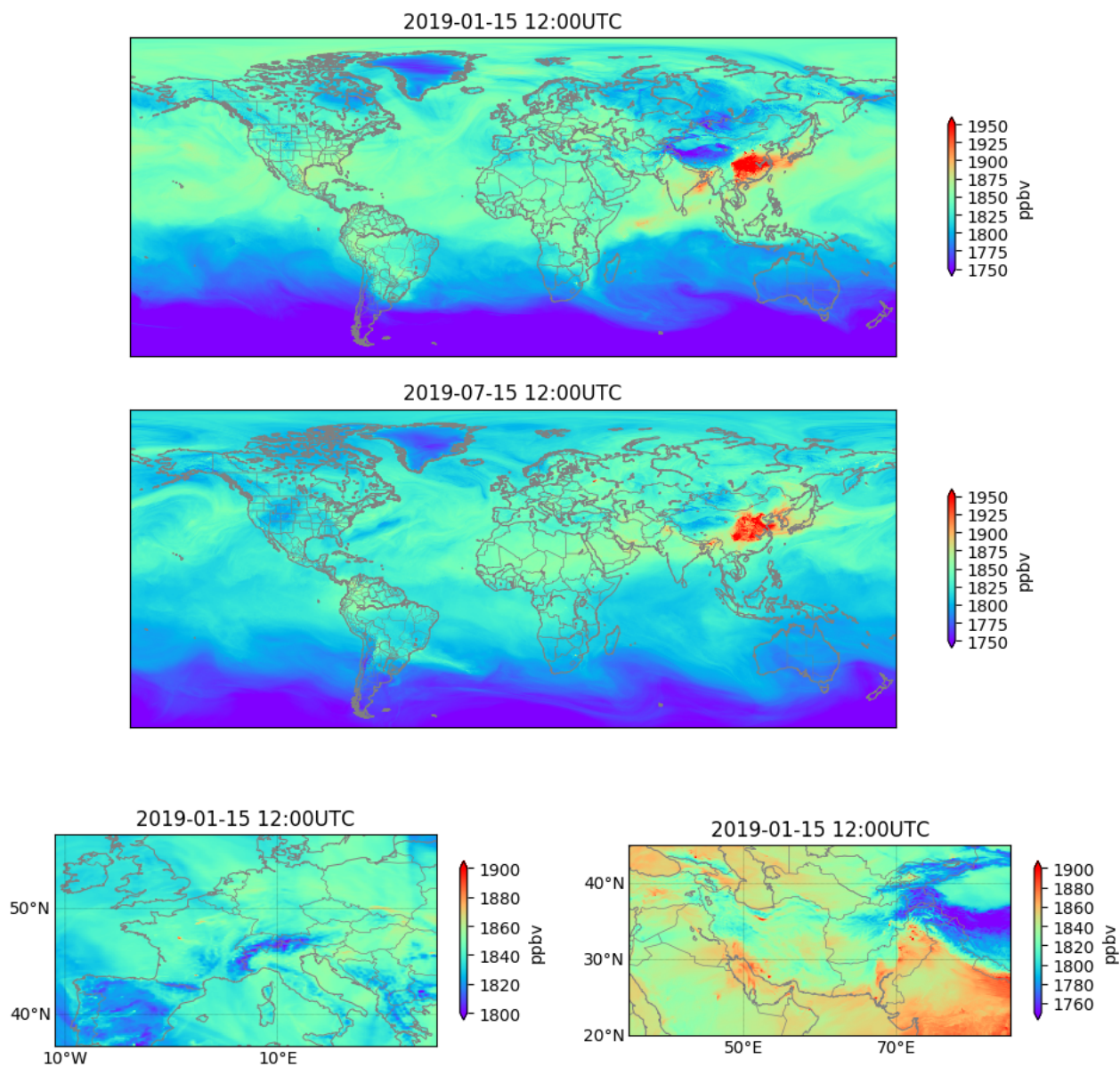
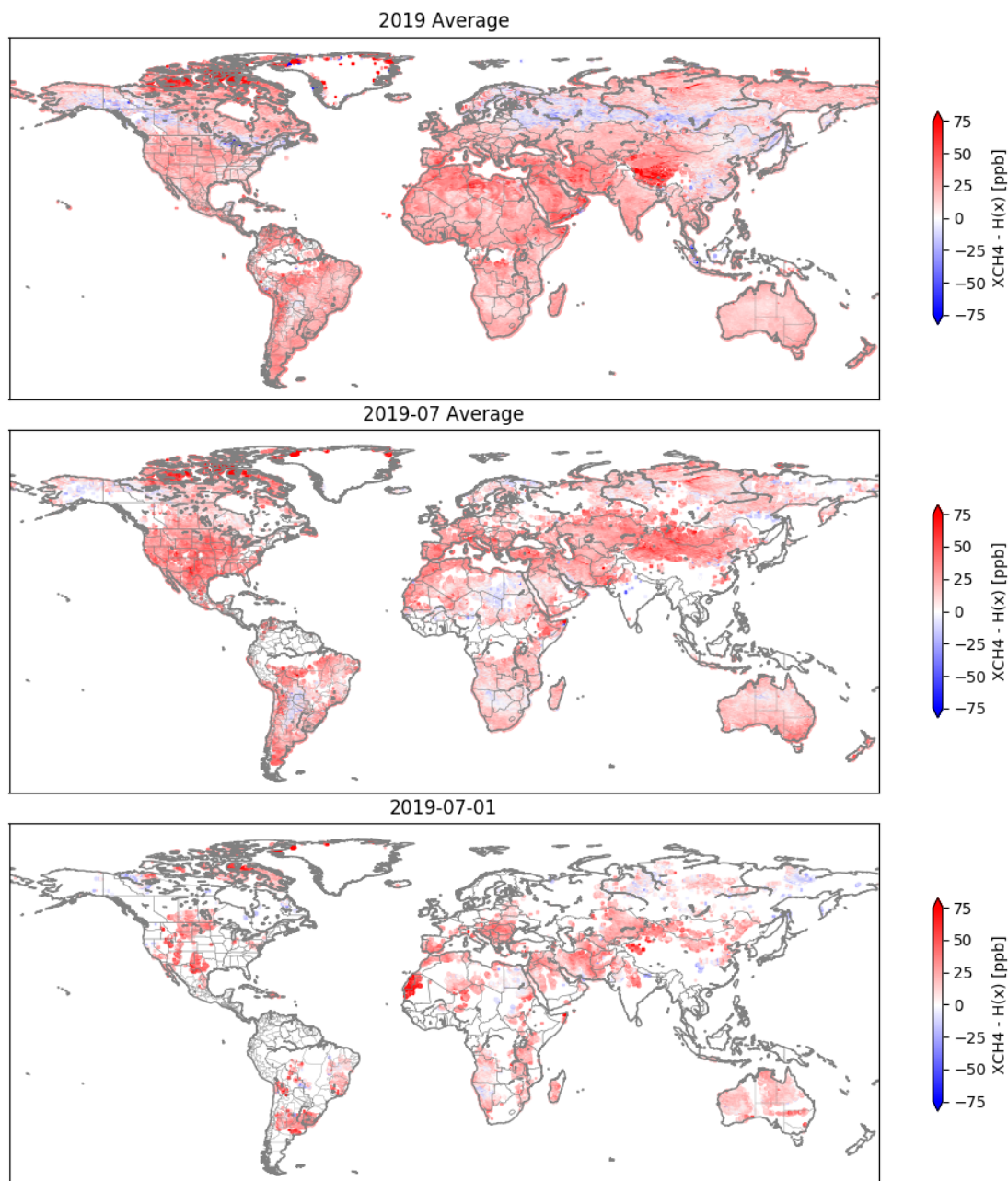


**Figure 4. Examples of combined next fluxes (positive only shown due to the logarithmic scale) that constitute the surface boundary conditions of the IFS high resolution CH<sub>4</sub> forecast. Global and regional scale examples for 2019-01-15 and 2019-07-05 at 12:00 UTC.**



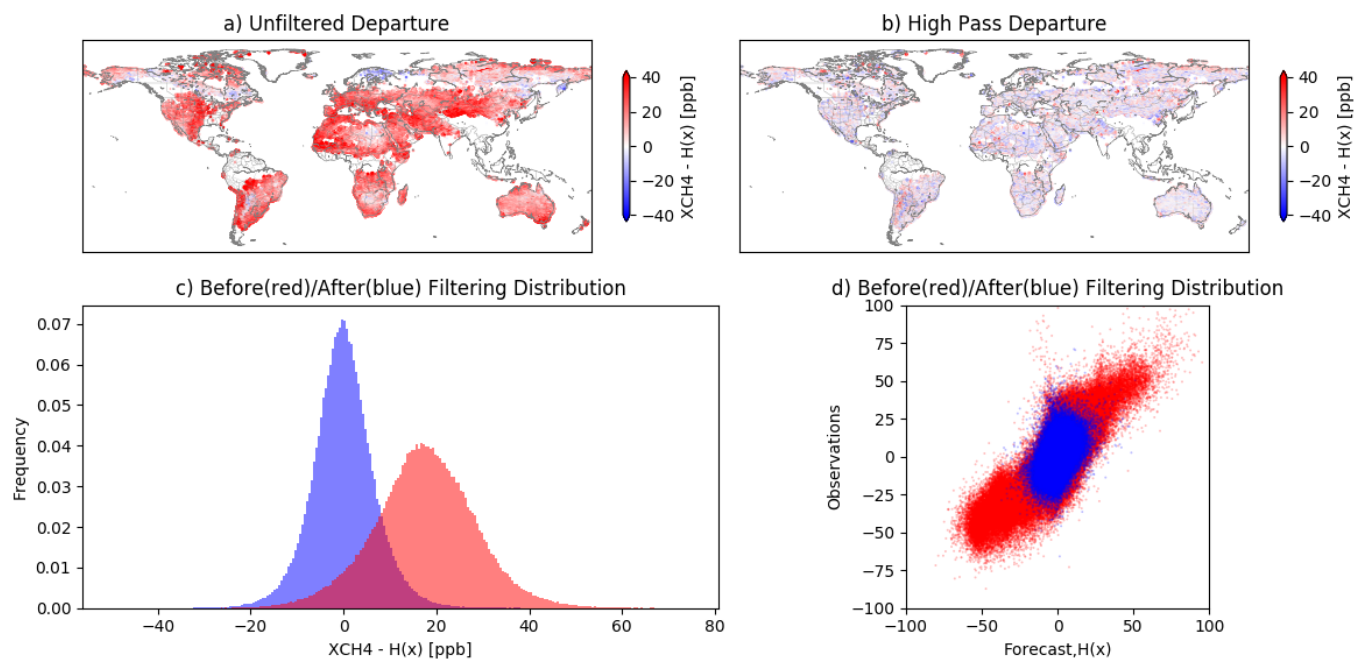
500

**Figure 5. Examples of outputs of the IFS high resolution CH<sub>4</sub> forecasts displaying snapshots at global and regional scale of the total column mean molar fractions for 2019-01-15 and 2019-07-15 at 12:00 UTC. Lower panels show parts of Europe (left) and Middle East (right).**



505

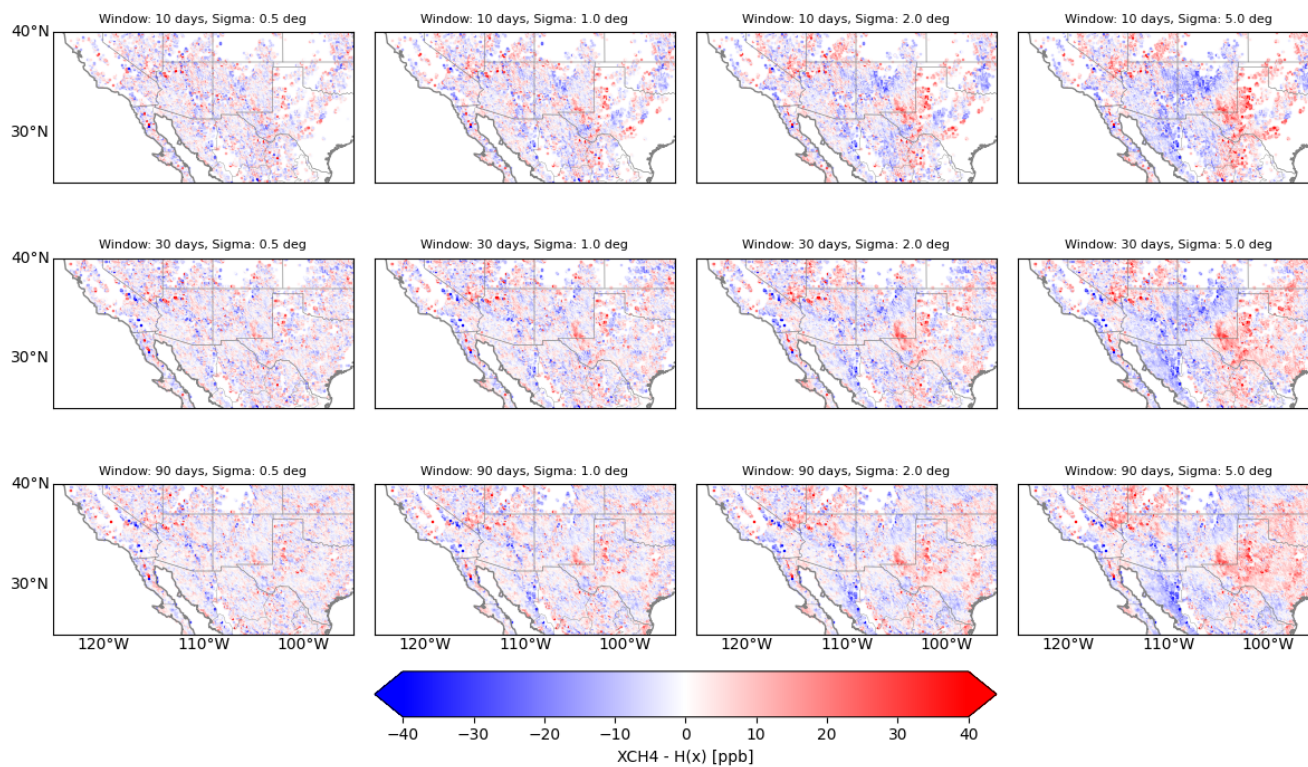
**Figure 6. Departures values computed with the observation displayed in figure 1, for the full year 2019, July 2019 and July 1st, 2019.**



510 **Figure 7. Example of the high pass filtering effect over a 30-day window with a 2° Gaussian kernel length scale. a) The unfiltered departures, b) the filtered departures, c) histograms comparing unfiltered (red) versus the filtered (blue) departures and d) 2D distributions in the observation and first-guess space for unfiltered (red) and filtered (blue) data points. Note that the unfiltered data points have been centred around the mean for this plot to make it comparable to the filtered distribution.**

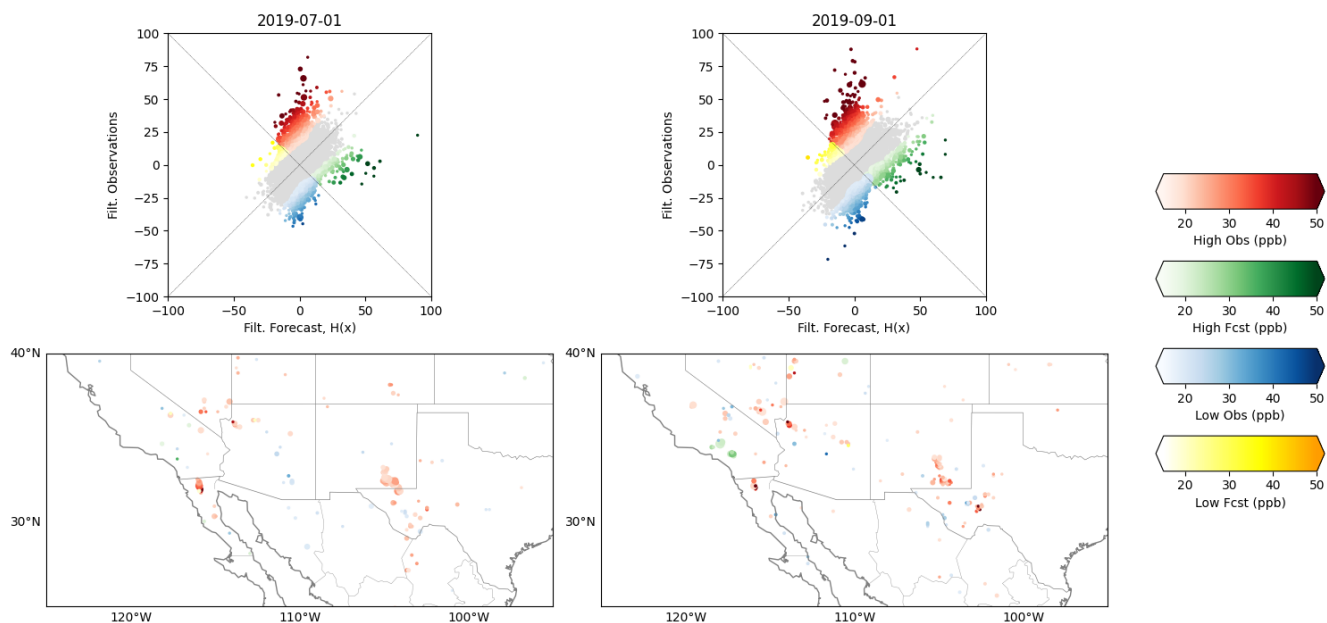


2019-07-01



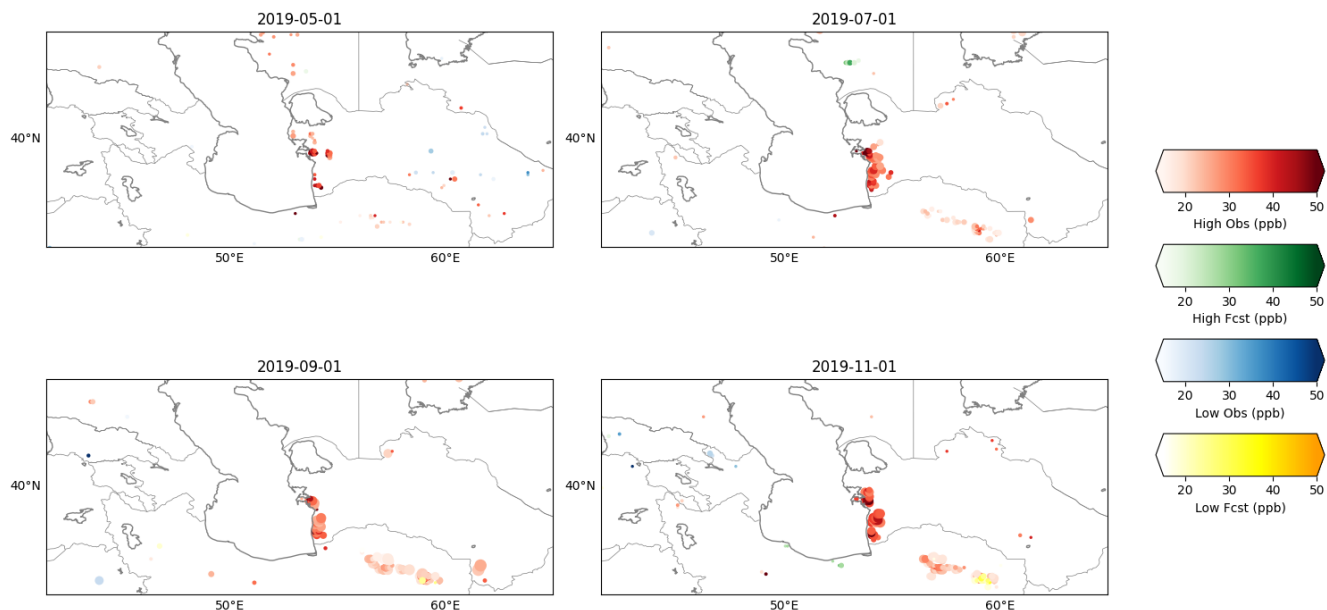
515

**Figure 8. High pass filtering sensitivity tests**



520

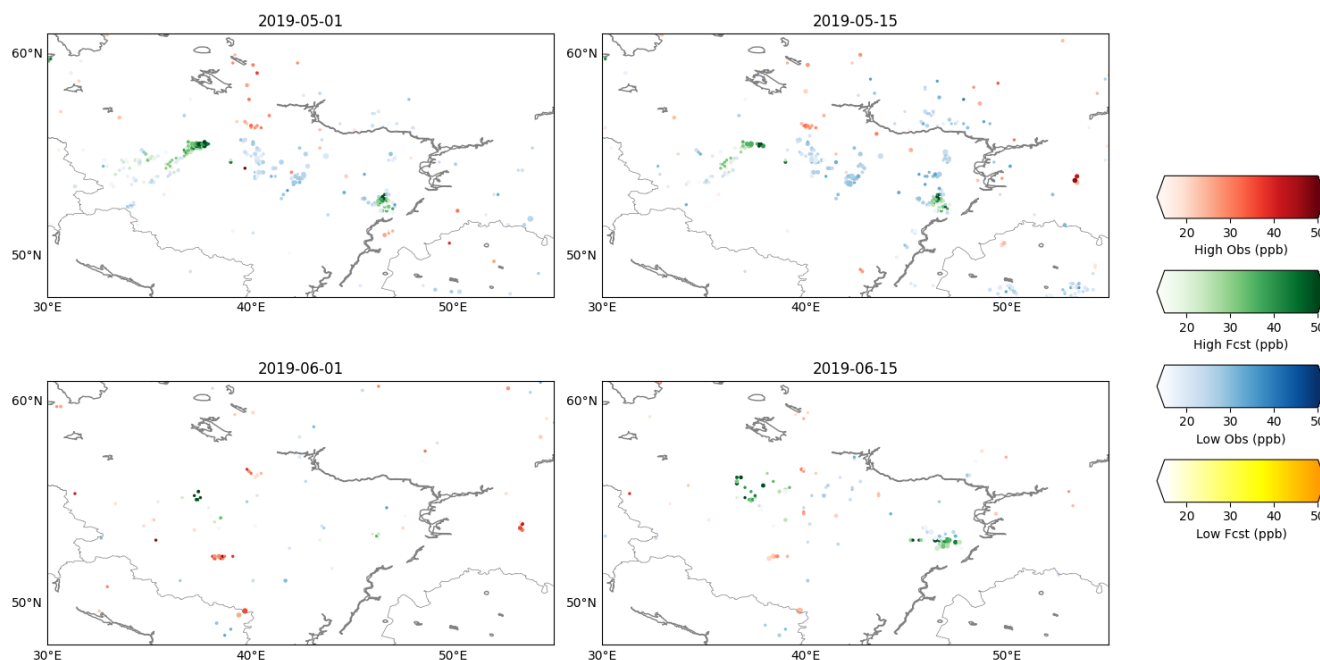
**Figure 9.** Examples of the outlier classification. **Top panels:** global distributions in the observation-first guess space for two different end dates of 30-day window (July 1st 2019 and September 1st 2019). **Colours illustrate the four different data classes.** **Bottom panels:** outlier classes localisation example over the south western US region. **Darker dots show larger departures. Larger dots indicate that more occurrences have been detected in the bin and time window.**



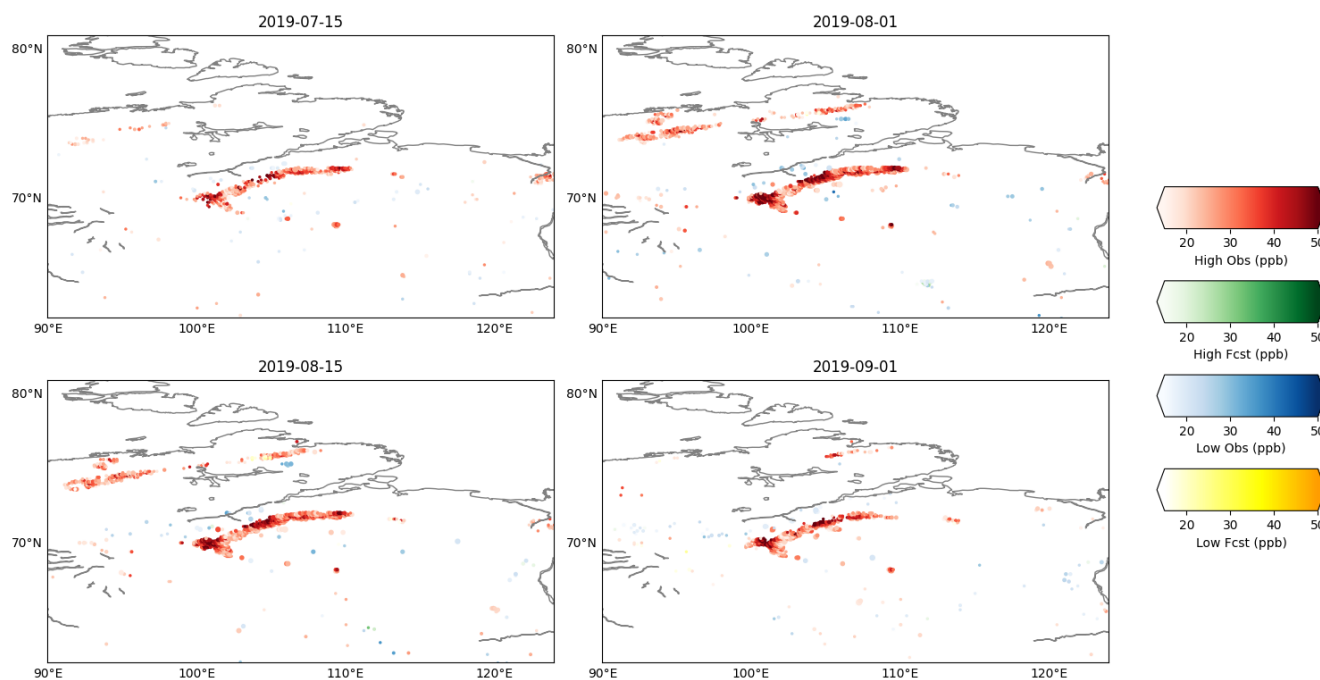


525

**Figure 10. Outlier detection and classification over Turkmenistan. Dates indicate the end date of the 30-day time window.**



**Figure 11. Outlier detection and classification over western Russia. Dates indicate the end date of the 30-day time window.**







530 **Figure 12. Outlier detection and classification over Siberia. Dates indicate the end date of the 30-day time window.**